

# Triple oxygen isotope insight into terrestrial pyrite oxidation

Jordon D. Hemingway<sup>a,1</sup>, Haley Olson<sup>a</sup>, Alexandra V. Turchyn<sup>b</sup>, Edward T. Tipper<sup>b</sup>, Mike Bickle<sup>b</sup>, and David T. Johnston<sup>a</sup>

<sup>a</sup>Department of Earth and Planetary Sciences, Harvard University, Cambridge, MA 02138; <sup>b</sup>Department of Earth Sciences, Cambridge University, Cambridge, UK CB2 1TN

This manuscript was compiled on January 26, 2020

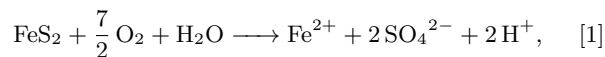
1 **The mass-independent minor oxygen isotope compositions ( $\Delta^{17}\text{O}$ )**  
2 **of atmospheric  $\text{O}_2$  and  $\text{CO}_2$  are primarily regulated by their rela-**  
3 **tive partial pressures,  $p\text{O}_2/p\text{CO}_2$ . Pyrite oxidation during chemical**  
4 **weathering on land consumes  $\text{O}_2$  and generates sulfate that is car-**  
5 **ried to the ocean by rivers. The  $\Delta^{17}\text{O}$  values of marine sulfate**  
6 **deposits have thus been proposed to quantitatively track ancient**  
7 **atmospheric conditions. This proxy assumes direct  $\text{O}_2$  incorpora-**  
8 **tion into terrestrial pyrite oxidation-derived sulfate, but a mechan-**  
9 **istic understanding of pyrite oxidation—including oxygen sources—**  
10 **in weathering environments remains elusive. To address this issue,**  
11 **we present sulfate source estimates and  $\Delta^{17}\text{O}$  measurements from**  
12 **modern rivers transecting the Annapurna Himalaya, Nepal. Sulfate**  
13 **in high-elevation headwaters is quantitatively sourced by pyrite ox-**  
14 **idation, but resulting  $\Delta^{17}\text{O}$  values imply no direct tropospheric  $\text{O}_2$**   
15 **incorporation. Rather, our results necessitate incorporation of oxy-**  
16 **gen atoms from alternative,  $^{17}\text{O}$ -enriched sources such as reactive**  
17 **oxygen species. Sulfate  $\Delta^{17}\text{O}$  decreases significantly when moving**  
18 **into warm, low-elevation tributaries draining the same bedrock lithol-**  
19 **ogy. We interpret this to reflect overprinting of the pyrite oxidation-**  
20 **derived  $\Delta^{17}\text{O}$  anomaly by microbial sulfate reduction and reoxida-**  
21 **tion, consistent with previously described major sulfur and oxygen**  
22 **isotope relationships. The geologic application of sulfate  $\Delta^{17}\text{O}$  as**  
23 **a proxy for past  $p\text{O}_2/p\text{CO}_2$  should consider both (i) alternative oxy-**  
24 **gen sources during pyrite oxidation and (ii) secondary overprinting**  
25 **by microbial recycling.**

atmospheric  $\text{O}_2$  | chemical weathering |  $\Delta^{17}\text{O}$  | Himalayas | sulfur cycle

1 **A**tmospheric molecular oxygen ( $\text{O}_2$ ) governs biogeochem-  
2 ical cycles, Earth's surface redox state, and the evolution  
3 of life;  $\text{O}_2$  partial pressure ( $p\text{O}_2$ ) has increased drastically in  
4 the geologic past in response to biologic and geologic drivers  
5 (1, 2). Despite this importance, quantitatively constraining  
6  $p\text{O}_2$  throughout Earth's history remains challenging due to  
7 a lack of direct proxies (2). Recently, the minor oxygen iso-  
8 tope composition ( $^{17}\text{O}/^{16}\text{O}$ , reported as  $\Delta^{17}\text{O}$ ; Materials and  
9 Methods) of geologically preserved minerals has been proposed  
10 as one such proxy (1, 3–8). This approach utilizes the fact  
11 that photochemical reactions between  $\text{O}_2$ , ozone ( $\text{O}_3$ ), and  
12 carbon dioxide ( $\text{CO}_2$ ) in the stratosphere generate anomalous,  
13 mass-independent  $^{17}\text{O}$  signatures that are mixed into the tro-  
14 posphere (9). In particular, tropospheric  $\text{O}_2$  carries a large  
15 negative  $\Delta^{17}\text{O}$  anomaly, the magnitude of which reflects: (i)  
16 the ratio of  $\text{O}_2$  to  $\text{CO}_2$  partial pressures ( $p\text{O}_2/p\text{CO}_2$ ), which  
17 determines the strength of the signal acquired during strato-  
18 spheric photochemistry, and (ii) the amount of  $\text{O}_2$  generated  
19 by oxygenic photosynthesis in the biosphere, which dilutes  
20 stratospheric inputs (1, 6). Thus, if  $p\text{CO}_2$  and biospheric pro-  
21 ductivity can be independently constrained, then tropospheric  
22  $\text{O}_2$   $\Delta^{17}\text{O}$  is potentially a direct and quantitative  $p\text{O}_2$  tracer.

23 Sulfate ( $\text{SO}_4^{2-}$ ) bearing minerals are particularly attractive

24 reservoirs for this method of reconstructing  $p\text{O}_2$  in the geologic  
25 past because oxidative pyrite ( $\text{FeS}_2$ ) weathering consumes  
26  $\text{O}_2$  (10, 11). If oxidation of pyrite contained in exhumed  
27 sedimentary rocks on land follows the reaction:



28 then contemporaneous tropospheric  $\text{O}_2$ —including its anomalous  
29  $^{17}\text{O}$  composition—could be directly incorporated into  
30 resulting sulfate (12). Isotopically labeled oxidation experi-  
31 ments support this idea;  $\approx 8\%$  to  $15\%$  of sulfate oxygen atoms  
32 have been shown to be sourced directly from dissolved  $\text{O}_2$  un-  
33 der well-oxygenated experimental conditions (12, 13). In light  
34 of these results and the fact that sulfate oxygen isotopes do  
35 not equilibrate with water on geologically relevant timescales,  
36 preserved barite ( $\text{BaSO}_4$ ), gypsum ( $\text{CaSO}_4$ ), and carbonate-  
37 associated sulfate  $\Delta^{17}\text{O}$  values have been used to reconstruct  
38  $p\text{O}_2/p\text{CO}_2$  throughout Earth's history (3–8, 14, 15). Such  
39 interpretations require two criteria to be met: (i) this direct  
40  $\text{O}_2$  consumption mechanism (Eq. 1) contributes a significant  
41 proportion of pyrite oxidation-derived sulfate and (ii) primary  
42  $\Delta^{17}\text{O}$  signals are not overprinted or diluted in the environ-  
43 ment prior to being preserved in the rock record. Tropospheric  
44  $\text{O}_2$   $^{17}\text{O}$  compositions in the geologic past are thus typically  
45 reconstructed using the most negative sulfate  $\Delta^{17}\text{O}$  value  
46 from a given geologic unit (i.e., least overprinted) and scaling  
47 by a  $\approx 8\%$  to  $15\%$   $\text{O}_2$  incorporation factor (7, 15).  
48

49 However, anoxic laboratory experiments and modern field  
50 observations complicate this picture. Specifically, both biotic  
51

## Significance Statement

Pyrite is oxidized during weathering to form dissolved sulfate that is carried to the ocean by rivers. This process is thought to incorporate atmospheric  $\text{O}_2$ -derived oxygen; geologically preserved sulfate has thus been proposed to directly trace past  $\text{O}_2$  isotope compositions. However, this mechanism has not been thoroughly tested in modern weathering environments. We show that dissolved sulfate in Himalayan rivers is predominantly derived from pyrite, yet its oxygen isotope compositions preclude direct  $\text{O}_2$  incorporation. Rather, alternative oxygen sources (e.g., reactive oxygen species) may be incorporated during oxidation, prompting reconsideration of the pyrite oxidation mechanism and the interpretation of geologically preserved sulfate as a direct  $\text{O}_2$  tracer.

Author contributions: J.D.H. and D.T.J. designed research; J.D.H. and H.O. performed research; A.V.T., E.T.T. and M.B. contributed new reagents or analytic tools; J.D.H., H.O. and D.T.J. analyzed data; J.D.H., H.O., A.V.T., E.T.T., M.B., and D.T.J. wrote the paper.

The authors declare no conflict of interest.

<sup>1</sup>To whom correspondence should be addressed. E-mail: jordon\_hemingwayfas.harvard.com

Fig. 1. (A) Marsiyandi basin map. Black lines delineate catchment areas upstream of each sample location. Background color represents elevation. Inset shows study location within Nepal. (B) Downstream evolution of elevation (blue line) and local MAT (red line) moving along the main-stem Marsiyandi. Also shown is the estimated fraction of sulfate derived from pyrite oxidation ( $f_{py}$ ) for each sample; tributaries are plotted at their confluence with the main-stem. Background shading indicates bedrock lithology. Symbols refer to: TSS tributaries (white squares), HHCS FI tributaries (gray circles), HHCS FII tributaries (light gray triangles), LHS tributaries (dark gray diamonds), and main-stem Marsiyandi (black triangles).

and abiotic experiments (10, 11, 13, 16, 17) imply that sulfate oxygen can be quantitatively sourced from meteoric water:



$\text{O}_2$  is then consumed indirectly during subsequent oxidation of  $\text{Fe}^{2+}$  to  $\text{Fe}^{3+}$ . If pyrite oxidation in the environment exclusively follows Eq. 2, then product sulfate  $^{17}\text{O}$  is decoupled from atmospheric  $\text{pO}_2/\text{pCO}_2$ . Recent studies using major oxygen and sulfur isotope compositions ( $^{18}\text{O}$ ,  $^{34}\text{S}$ ; Materials and Methods) suggest that pyrite oxidation in some modern river systems occurs in suboxic groundwater aquifers and quantitatively incorporates meteoric water-derived oxygen (18, 20). Consistent with this interpretation, detailed studies of shale bedrock drill cores indicate that pyrite oxidation occurs in low- $\text{O}_2$  pores and microfractures within a deep, sharp reaction front independent of erosion rate (21). Such results raise the question as to why direct  $\text{O}_2$  incorporation into sulfate is evident in the geologic past but is apparently absent from modern pyrite weathering environments. Furthermore, pyrite oxidation must proceed via 1-electron transfer steps regardless of the exact mechanism involved (11, 22, 23), raising the possibility that reactive oxygen species (ROS; e.g.,  $\text{H}_2\text{O}_2$ ,  $\text{O}_2$ ,  $\text{OH}^\cdot$ ) may provide additional, isotopically unique oxygen sources to sulfate (24, 25). ROS incorporation could help to reconcile modern and ancient observations, but its environmental importance remains unknown.

To provide new insight, we constrain the sulfate budget in a suite of highly erosive mountainous rivers. Building upon previous work reporting  $^{18}\text{O}$  and  $^{34}\text{S}$  evolution (20), we document sulfate source and  $^{17}\text{O}$  values for samples collected throughout the Marsiyandi River basin, Annapurna Himalaya, Nepal. These results update our understanding of orogenic sulfate oxygen isotope systematics, with implications for modern weathering budgets and geologic  $\text{pO}_2/\text{pCO}_2$  reconstructions.

**Study Setting.** The Marsiyandi River is located in the Southern Flank of the Annapurna Himalaya, Central Nepal (Fig. 1A). Headwaters drain the Tethyan Sedimentary Series (TSS); although some Manaslu granite exposures exist within our study region, bedrock is primarily described as a continental margin sequence containing variably metamorphosed limestone and siliclastics with interbedded pyrite-rich black shales (26, 28). The TSS lies entirely within the Himalayan orogenic rain shadow; vegetation is sparse (29) and mean annual precipitation (MAP) never exceeds  $1000 \text{ mm yr}^{-1}$  (average  $500 \text{ mm yr}^{-1}$ ) (30). Mean annual temperature (MAT) within the TSS ranges from  $10^\circ\text{C}$  in the highest elevations to near

$15^\circ\text{C}$  in the lowest elevations (Fig. 1B). Downstream of the TSS, the Higher Himalayan Crystalline Series (HHCS) contains two main bedrock units: Formation I (FI), dominated by silicate gneiss, and Formation II (FII), dominated by calc-silicate metamorphic rocks (26, 31). MAP increases markedly due to the influence of the Indian Summer Monsoon, reaching  $2500 \text{ mm yr}^{-1}$  (30), whereas MAT exhibits only modest increases (Fig. 1B). Further downstream, the Lesser Himalayan Series (LHS) is described as undifferentiated low- to medium-grade metasedimentary and metavolcanic rocks (27) and by MAP and MAT values near those within the HHCS. Importantly, evaporitic successions have never been reported in Central Nepal (29).

## Results

Samples were collected in May (pre-monsoon) and September (monsoon season) 2002 across a 120 km transect starting at the Marsiyandi River headwaters in the TSS (5000 m elevation) and ending in the LHS near the base of the Himalaya (750 m elevation; Fig. 1B) (29, 33, 35). Most samples were collected from small tributaries draining single lithologies (median catchment area =  $20 \text{ km}^2$ ; Table S2) and are independent of one another. Tributaries span a range of catchment slopes (24:0 to 41:1 deg), MAP ( $407$  to  $1330 \text{ mm yr}^{-1}$ ), MAT ( $10$  to  $15^\circ\text{C}$ ), and glacial extent (0 to 46 % by area; Table S2). This approach allows us to isolate the effect of geomorphic/environmental changes on riverine chemistry while holding lithology and catchment area roughly constant (36). To investigate main-stem evolution, we additionally report results from the Marsiyandi River at 4 locations throughout the basin.

**Sulfate Sources.** Sulfate source contributions including atmospheric inputs and carbonate, evaporite, granite, and shale weathering were estimated using a conservative tracer mixing model and previously published major ion concentrations (Materials and Methods) (29). Results indicate that the fraction of riverine sulfate derived from pyrite oxidation in shale, termed  $f_{py}$ , ranges from 40 to 100 % (Fig. 1B).  $f_{py}$  is highest in sulfate-rich TSS tributaries, ranging from 60 to 100 % and averaging  $91 \pm 11\%$  ( $n = 25$ ; Table S1). Slightly lower  $f_{py}$  values in the most downstream TSS samples could result from partial HHCS or Manaslu granite bedrock exposure in these tributaries (29). Across the entire sample set,

\* Chloride-rich hydrothermal hot springs along fault zones do suggest the presence of basinal brines or buried halite (33, 37). However, hot springs are deficient in both  $\text{SO}_4^{2-}$  and  $\text{Ca}^{2+}$  relative to  $\text{Cl}^-$  and  $\text{Na}^+$  (37), indicating minimal contribution of gypsum dissolution to hydrothermal solutes and thus precluding evaporite weathering as a major driver of observed sulfate trends.

139  $p_{py}$  decreases moving downstream (slope =  $0.003\% \text{ km}^{-1}$ ,  
 140  $p = 6.5 \times 10^{-5}$ ), largely due to the sharp drop within trib-  
 141 utaries draining HHCS FII calc-silicate metamorphic rocks.  
 142 This drop coincides with the Southern Tibetan Detachment  
 143 System and the Main Central Thrust (35) and is likely driven  
 144 by contributions from limestone weathering in this region, as  
 145 suggested by our weathering model results (Table S1). In con-  
 146 trast, when considering only TSS samples that are su ciently  
 147 upstream of potential HHCS and Manaslu granite in uence  
 148 ( $40 \text{ km}$  from the the source) (29),  $p_{py}$  remains near 100%  
 149 and does not correlate with downstream distance ( $p > 0.05$ ).  
 150 Importantly, results account for precipitation-derived sulfate,  
 151 including anthropogenic sources (i.e., acid rain). These inputs  
 152 never exceed 11% of total sulfate in any sample, averaging  
 153 only 2.0–2.5% ( $n = 38$ ) across the entire sample set and  
 154 1.0–1.1% ( $n = 25$ ) within the TSS, consistent with low mea-  
 155 sured sulfate concentrations in Himalayan rain water (38, 39).  
 156 We thus primarily limit our sulfate  $^{17}\text{O}$  isotope measurements  
 157 to upstream TSS catchments.

158 Sulfate Isotopes. Riverine sulfate  $^{17}\text{O}$  ranges from 0.041  
 159 to  $0.180 \pm \text{VSMOW}$  (average =  $0.117 \pm 0.038 \pm \text{VSMOW}$ ;  
 160  $n = 29$ ; Table S1) and exhibits a signi cant decrease moving  
 161 downstream (slope =  $0.001 \pm \text{km}^{-1}$ ;  $p = 3.8 \times 10^{-3}$ ;  $R^2 =$   
 162  $0.35$ ; Fig. S1). Sulfate  $^{17}\text{O}$  is negatively correlated with  
 163 both  $^{18}\text{O}$  (slope =  $0.005 \pm \text{‰}^{-1}$ ;  $p = 3.8 \times 10^{-3}$ ;  $R^2 =$   
 164  $0.44$ ; Fig. 2A) and  $^{34}\text{S}$  (slope =  $0.002 \pm \text{‰}^{-1}$ ;  $p = 1.6$   
 165  $\times 10^{-4}$ ;  $R^2 = 0.41$ ; Table S1). Because sulfate oxygen can be  
 166 sourced directly from water (Eq. 2) (10, 11, 16, 17, 40), we  
 167 additionally report offsets between sulfate and concomitant  
 168 river water  $^{18}\text{O}$  and  $^{17}\text{O}$ , termed  $^{18}\text{O}$  and  $^{17}\text{O}$   
 169 (Fig. 2B; Materials and Methods). Water  $^{18}\text{O}$  was measured  
 170 directly (20), whereas  $^{17}\text{O}$  was calculated using the global  
 171 meteoric water line (32).  $^{17}\text{O}$  ranges from  $0.033$  to  
 172  $0.103 \pm \text{‰}$  (average =  $0.048 \pm 0.034 \pm \text{‰}$ ;  $n = 26$ ; Table S1) and  
 173 displays a statistically signi cant decrease with increasing  
 174  $^{18}\text{O}$  (slope =  $0.008 \pm \text{‰}^{-1}$ ;  $p = 8.3 \times 10^{-4}$ ;  $R^2 = 0.39$ ;  
 175 Fig. 2B). In contrast, both  $^{17}\text{O}$  and  $^{18}\text{O}$  values do  
 176 not correlate with  $p_{py}$  estimates nor with estimated fractional  
 177 dolomite, gneiss/granite, limestone, or evaporite end-member  
 178 weathering contributions ( $p > 0.05$ ). Unlike  $p_{py}$ , which is  
 179 largely stable near 100% within the TSS, sulfate  $^{17}\text{O}$  values  
 180 in tributaries draining this region display large and systematic  
 181 decreases moving downstream (Fig. S1).

Fig. 2. Oxygen isotope compositions. (A) colored points:  
 $^{17}\text{O}$  vs.  $^{18}\text{O}$  scatter plot for all sulfate samples; gray line:  
 Marsiyandi basin river water isotope array. Water  $^{18}\text{O}$  was  
 measured directly (20) and  $^{17}\text{O}$  was calculated using the  
 global meteoric water line (32). (B) Scatter plot of  $^{17}\text{O}$   
 vs.  $^{18}\text{O}$ , the offsets between sulfate and concomitant  
 river water  $^{17}\text{O}$  and  $^{18}\text{O}$  (Materials and Methods). For  
 both panels, symbol colors refer to the estimated fraction  
 of sulfate derived from pyrite oxidation ( $p_{py}$ ) and shapes  
 represent: TSS tributaries (squares), LHS tributaries (dia-  
 monds), and the main-stem Marsiyandi (triangles).  $^{17}\text{O}$   
 and  $^{18}\text{O}$  uncertainty ( $\pm 1$ ) is the long-term instru-  
 ment reproducibility (Materials and Methods);  $^{18}\text{O}$  and  
 $^{17}\text{O}$  uncertainty is smaller than marker points (20). Both  
 panels show that sulfate is generally enriched in  $^{17}\text{O}$  relative  
 to meteoric water, opposite of what would be expected from  
 direct atmospheric  $\text{O}_2$  incorporation.

## Discussion

182  
 183 Fluvial Sulfate Oxygen Source. We observe spatially coherent  
 184 sulfate oxygen isotope signals throughout the Marsiyandi River  
 185 basin. Headwater sulfate exhibits large, positive  $^{17}\text{O}$  val-  
 186 ues ( $^{17}\text{O} = 0.10 \pm \text{‰}$ ) as well as  $^{18}\text{O}$  near that of local  
 187 meteoric water ( $^{18}\text{O} = 5 \pm \text{‰}$ ). Consistent with previous  
 188 observations based on sulfate  $^{18}\text{O}$  from a suite of global rivers  
 189 (18–20), these results imply that pyrite weathering in mountain-  
 190 ous headwaters occurs primarily within suboxic groundwater  
 191 aquifers. Sulfate  $^{17}\text{O}$  compositions indicate no appreciable  $\text{O}_2$   
 192 incorporation during pyrite oxidation (Eq. 1). Any  $\text{O}_2$  con-  
 193 tribution would produce sulfate with  $^{17}\text{O}$  below the meteoric  
 194 water line (i.e.,  $^{17}\text{O} < 0$ ) since  $^{17}\text{O} = 0.5 \pm \text{‰}$  VSMOW  
 195 in modern tropospheric  $\text{O}_2$  (6, 9). However, the opposite is  
 196 observed (Fig. 2B). Furthermore, mass-dependent isotope  
 197 fractionation associated with anoxic pyrite weathering (Eq.  
 198 2) likely cannot explain observed  $^{17}\text{O}$  enrichment since this  
 199 would require a mass law of 0.54 to 0.55, considerably  
 200 higher than any known low-temperature microbial or abiotic  
 201 processes (1, 41). Rather, positive  $^{17}\text{O}$  values require  
 202 either (i) overprinting by atmospherically derived (precipita-  
 203 tion or aerosol) sulfate inputs (1, 41) or (ii) an additional,  
 204  $^{17}\text{O}$ -enriched oxygen source that is incorporated into sulfate  
 205 during pyrite oxidation.

206 We first consider atmospheric inputs. Many oxygen-bearing  
 207 gases carry positive  $^{17}\text{O}$  anomalies that can be transferred  
 208 to sulfate in the atmosphere. For instance, aqueous-phase  
 209  $\text{SO}_2$  oxidation by  $^{17}\text{O}$ -enriched  $\text{H}_2\text{O}_2$  or  $\text{O}_3$  in the atmosphere  
 210 generates sulfate in rainwater and aerosols with positive  $^{17}\text{O}$   
 211 values (41, 42). It is therefore possible that aerosol and/or  
 212 rainwater inputs contribute to observed riverine sulfate signals.  
 213 However, although correct in the required  $^{17}\text{O}$  directionality,  
 214 atmospheric deposition alone fails to explain our results for  
 215 three reasons:

216 (1) According to our conservative tracer mixing model,  
 217 precipitation accounts for 2.0–2.5% of total sulfate in the  
 218 entire sample set and only 1.0–1.1% within the TSS, where  
 219  $^{17}\text{O}$  values are highest. If we assume all pyrite oxidation-  
 220 derived sulfate follows Eq. 2 with no mass-independent  
 221 isotope fractionation, then mass balance considerations re-  
 222 quire precipitation-derived sulfate with  $^{17}\text{O}$  values up to  
 223  $9 \pm \text{‰}$  VSMOW (higher if any contribution by Eq. 1 is in-  
 224 voked). This is nearly an order of magnitude higher than  
 225 measured rainwater sulfate  $^{17}\text{O}$  (41).

226 Still, it has previously been shown that 25% of sulfate

227 in Rocky Mountain headwater streams draining sulfate-poor  
 228 gneiss and granite lithologies can be sourced from atmospheric  
 229 deposition in snowpack (43). However, Marsiyandi headwater  
 230 stream sulfate concentrations are 20% higher than those of  
 231 Ref. (43). Thus, if we assume snowpack sulfate  $^{17}\text{O}$  values  
 232 are similar in the Himalaya and Rocky Mountains (i.e., 0.8‰  
 233 to 1.5‰), then mass balance considerations would require  
 234 snowpack sulfate concentrations of 150  $\mu\text{M}$ . This is an order  
 235 of magnitude higher than reported Himalayan precipitation  
 236 and Rocky Mountain snowpack concentrations (38, 39, 43).

237 (2) Riverine sulfate  $^{18}\text{O}$ ,  $^{34}\text{S}$ , and  $^{17}\text{O}$  trends are identical  
 238 during pre-monsoon and monsoon seasons despite differences  
 239 in air mass trajectories, precipitation amounts, and the  
 240 importance of wet vs. dry deposition. In particular, we would  
 241 expect significantly lower  $^{17}\text{O}$  during the dry pre-monsoon  
 242 season since atmospheric sulfate produced by gas-phase  $\text{H}_2\text{SO}_4$   
 243 does not carry mass-independent  $^{17}\text{O}$  signal (42). Similarly,  
 244 if aerosol deposition were driving observed trends, then  
 245 we would expect a much larger positive signal during the  
 246 monsoon season when air masses cross the (heavily polluted)  
 247 Indian subcontinent (41). This is not observed. Rather, for  
 248 sites in which pre-monsoon and monsoon sampling can be compared  
 249 directly, there exists no statistically significant seasonal  
 250 difference in either sulfate  $^{18}\text{O}$  (May–September: 0.1–2.8  
 251 ‰;  $n = 4$ ) or sulfate  $^{17}\text{O}$  (May–September:  
 252 0.002–0.030 ‰;  $n = 3$ ).

253 (3) Fluvial sulfate concentrations and  $^{17}\text{O}$  values both  
 254 decrease as MAP increases moving downstream, opposite of  
 255 the expected atmospheric deposition trend. Highly erosive tributaries  
 256 draining pyrite-rich TSS lithologies exhibit particularly  
 257 positive  $^{17}\text{O}$  values, up to 0.180‰ VSMOW, despite receiving  
 258 only 400  $\text{mm yr}^{-1}$  MAP (Table S2). Similar to snowpack,  
 259 it is possible that glacial meltwater contributes atmospheric  
 260 precipitation- or aerosol-derived sulfate to headwater streams  
 261 (44). However, we observe no statistical correlation between  
 262 sulfate  $^{17}\text{O}$  and aerial glacier extent across our sample set  
 263 ( $p > 0.05$ ; Table S1–S2), suggesting that glacier meltwater  
 264 contributions alone cannot explain observed trends. Thus,  
 265 while atmospheric deposition can contribute to fluvial sulfate  
 266 with positive  $^{17}\text{O}$  values (43), such contributions are likely  
 267 negligible in the Marsiyandi River basin.

268 Marsiyandi River headwater sulfate is thus quantitatively  
 269 rock-derived. The question then arises: what is the source  
 270 of  $^{17}\text{O}$ -enriched oxygen to pyrite oxidation-derived sulfate?  
 271 Pyrite oxidation proceeds via 1-electron transfer steps occurring  
 272 at anode sites on the mineral surface and thus involves  
 273 oxygen-bearing sulfur intermediate species ( $\text{S}_2\text{O}_2^{2-}$ ,  $\text{S}_3\text{O}_6^{2-}$ ,  
 274  $\text{SO}_3^{2-}$ ) (11). Sulfite ( $\text{SO}_3^{2-}$ ), the most likely terminal precursor  
 275 to sulfate, rapidly reaches isotopic equilibrium with water  
 276 (46), raising the possibility that pyrite oxidation-derived sulfate  
 277  $^{17}\text{O}$  is buffered to water regardless of the original oxygen  
 278 source. However, the measured equilibrium sulfite-water  $^{18}\text{O}$   
 279 effect (46) is significantly larger than headwater  $^{18}\text{O}$  values  
 280 observed here (0.5‰; Fig. 2B), suggesting sulfite-water  
 281 isotope equilibrium cannot explain observed  $^{18}\text{O}$  and  $^{17}\text{O}$   
 282 trends.

283 Rather, we hypothesize that ROS isotope signatures are  
 284 incorporated into pyrite oxidation-derived sulfate, consistent  
 285 with laboratory experimental results (10, 11, 16, 17, 22, 40).  
 286 Electrochemical studies treat pyrite as a semiconductor with  
 287 a sulfur anode and an iron cathode; this model states that

Fig. 3. Sulfate oxygen source mixing diagram. White circles are measured riverine sulfate oxygen isotope compositions (Fig. 2A); blue circle is the high-elevation headwater meteoric water composition. Gray region is a mixing array between high-elevation meteoric water and the measured range of precipitation-derived  $\text{H}_2\text{O}_2$  compositions (24); shading represents fraction of  $\text{H}_2\text{O}_2$  contribution. Red region is a hypothesized MSR fractionation array starting from a "primary" headwater sulfate composition; shading represents range of possible MSR values (45). The black dotted line is a mixing line between the same starting composition and tropospheric  $\text{O}_2$ . The primary composition used to define this mixing space was chosen such that the majority of data fall within the bounds defined by primary sulfate, MSR fractionation, and  $\text{O}_2$  incorporation. Measured sulfate compositions cannot be explained as a binary mixing between meteoric water and tropospheric  $\text{O}_2$ , especially in  $^{17}\text{O}$ -enriched headwater TSS tributaries.

288 sulfate oxygen is quantitatively derived from  $\text{H}_2\text{O}$  or other  
 289  $\text{O}(\text{II})$  bearing species, whereas  $\text{O}_2$  is reduced via ROS inter-  
 290 mediates on iron cathode sites (22, 23). Furthermore, pyrite  
 291 surfaces are almost always covered in  $\text{Fe}(\text{III})$ -hydroxide patches  
 292 (11, 47); these patches have been shown to disproportionate  
 293  $\text{H}_2\text{O}_2$ , generating  $\text{O}_2$  and  $\text{H}_2\text{O}$  with unique isotope signatures  
 294 relative to those of bulk fluid (23). If  $\text{H}_2\text{O}_2$ -derived  $\text{H}_2\text{O}$  is  
 295 adsorbed onto pyrite surfaces, then these molecules could be  
 296 preferentially incorporated into neighboring anode sulfur sites  
 297 despite their low molarity relative to bulk water. In addition to  
 298 explaining the origin of  $^{17}\text{O}$ -enriched sulfate, this mechanism  
 299 could potentially reconcile the apparent non-stoichiometric  
 300  $\text{O}_2$  incorporation observed in isotope labeling pyrite oxidation  
 301 experiments (i.e., values other than 25, 50, 75, or 100%  
 302  $\text{O}_2$ -derived) (12, 13). That is, if isotopically labeled  $\text{O}_2$  is  
 303 reduced to  $\text{H}_2\text{O}$  via ROS intermediates on pyrite surfaces,  
 304 then the apparent incorporation of this signature into sulfate  
 305 would depend on the relative amount of adsorbed surface sites  
 306 occupied by these molecules and would not be constrained by  
 307 sulfate oxygen stoichiometry.

308 There are at least two pathways by which ROS incorporation  
 309 could explain our observed positive sulfate  $^{17}\text{O}$  values:  
 310 (1) in situ production of  $^{17}\text{O}$ -enriched  $\text{H}_2\text{O}_2$  during  $\text{O}_2$  reduction  
 311 on pyrite surfaces, or (2) delivery of atmospheric  
 312  $\text{H}_2\text{O}_2$  to the site of pyrite oxidation, for example by rainwater  
 313 (24, 25, 42). Although the mass-dependent fractionation relationships  
 314 are currently not known for any step of the pyrite  
 315 oxidation mechanism, the analogous  $\text{H}_2\text{O}_2$ -producing Mehler  
 316 reaction has been shown to follow 0.50 (48). If  $\text{O}_2$  reduction  
 317 on pyrite surfaces follows a similar value as that of the  
 318 Mehler reaction, then this process would generate  $^{17}\text{O}$ -enriched  
 319  $\text{H}_2\text{O}_2$  that could be disproportionated and incorporated into  
 320 sulfate. Future research is clearly needed to constrain these

Fig. 4. Sulfate major isotope compositions. Colored points:  $^{18}\text{O}$  vs.  $^{34}\text{S}$  for all samples in Ref. (20). Symbol colors represent  $\delta_{\text{py}}$  values and shapes refer to: TSS tributaries (squares), HHCS FI tributaries (circles), HHCS FI tributaries (right-pointing triangles), LHS tributaries (diamonds), and the main-stem Marsiyandi (down-pointing triangles). Histograms: literature compilations of all reported  $^{18}\text{O}$  and  $^{34}\text{S}$  values from global rivers (Table S4; Materials and Methods). Marsiyandi River basin  $^{18}\text{O}$  and  $^{34}\text{S}$  compositions span nearly the entire global range and approach global median values moving downstream.

fractionation factors.

Alternatively, it has been shown that rainwater contains up to  $30\mu\text{M}$   $\text{H}_2\text{O}_2$  with  $^{17}\text{O}$  values near  $1.0\pm$  VSMOW (25). A substantial fraction of this  $\text{H}_2\text{O}_2$  is transferred to river water; measured concentrations reach  $150\text{ nM}$  (49, 50). If we assume (i) pyrite oxidation-derived sulfate oxygen is sourced from a mixture of river water and  $\text{H}_2\text{O}_2$ , (ii) rainwater  $\text{H}_2\text{O}_2$   $^{17}\text{O}$  values reported in the literature (25) are generally representative, and (iii) disproportionation and incorporation into sulfate molecules does not impart a mass-independent anomaly (12), then atmospherically derived  $\text{H}_2\text{O}_2$  could contribute 7 to 15 % of sulfate oxygen in Marsiyandi headwaters (Fig. 3). This result satisfies both  $^{18}\text{O}$  and  $^{17}\text{O}$  observations. Still, it remains unclear how and to what extent rainwater  $\text{H}_2\text{O}_2$  would survive to the site of pyrite oxidation; while this estimate based on the limited existing literature ROS  $^{17}\text{O}$  data (24) appears reasonable, we emphasize that we do not quantitatively trust these results.

Regardless of the exact delivery mechanism invoked, pyrite oxidation-derived sulfate oxygen in mountainous rivers must be sourced primarily from meteoric water with supplemental contributions from a  $^{17}\text{O}$ -enriched source. Electrochemical models and limited  $^{17}\text{O}$  measurements suggest this source is likely  $\text{H}_2\text{O}_2$ , but other ROS (e.g.,  $\text{O}_2$ ,  $\text{OH}^\cdot$ ) or oxidants (e.g.,  $\text{NO}_3^-$ ) containing positive  $^{17}\text{O}$  anomalies (51) could instead be driving observed signals. Future work is needed to provide detailed constraints on the importance of each of these species and pathways.

Downstream Evolution and Implications for Global Sulfur Budgets. Moving downstream, riverine sulfate becomes enriched in  $^{34}\text{S}$  and  $^{18}\text{O}$  and loses its positive  $^{17}\text{O}$  anomaly. This transition occurs within tributaries draining the TSS and is therefore unlikely to result from changes in weathering lithol-

ogy (Fig. S1). Rather, microbial sulfate reduction (MSR) is more active in lower elevation, warmer catchments overlain by thicker, organic-rich soils. In particular, hyporheic zones anoxic bank and bed sediments that are in hydrologic contact with river water (52) are known to host highly active sulfate-reducing bacterial communities (53) and are thus a likely locus of MSR in the Marsiyandi River basin. MSR followed by sul de precipitation or outgassing will increase residual sulfate  $^{34}\text{S}$  and  $^{18}\text{O}$  values independent of the original sulfate source; the observed isotope fractionations are consistent in magnitude and direction with laboratory studies (54) and with previous field measurements (55). This mechanism is further supported by the strong positive relationships between local MAT and both sulfate  $^{34}\text{S}$  ( $p = 2.9 \times 10^{-7}$ ;  $R^2 = 0.53$ ) and  $^{18}\text{O}$  values ( $p = 1.6 \times 10^{-6}$ ;  $R^2 = 0.49$ ; Table S1, S2).

Resulting biogenic sul de could be lost via  $\text{H}_2\text{S}$  outgassing from anoxic soils or retained locally as secondarily precipitated sul de minerals and/or organic sulfur (56). For example, previous studies have utilized a network of bore holes in a temperate, first order stream to show that MSR can lead to an order-of-magnitude  $\text{H}_2\text{S}$  supersaturation with respect to sul de mineral precipitation ( $\text{FeS}$  and  $\text{FeS}_2$ ) in anoxic river bank sediments (53). The interpretation that sulfate reduction and subsequent loss is driving observed isotope trends is supported by strong negative correlations between sulfate concentration and both sulfate  $^{34}\text{S}$  ( $p = 1.6 \times 10^{-10}$ ;  $R^2 = 0.69$ ) and  $^{18}\text{O}$  values ( $p = 3.6 \times 10^{-9}$ ;  $R^2 = 0.63$ ; Table S1). If glacially carved valleys are being actively infilled by sediment in this region, then non-steady-state growth of secondarily precipitated sulfur reservoirs could exacerbate observed downstream sulfate isotope enrichments; this is likely occurring given such large  $^{34}\text{S}$  variability observed here (Fig. 4). However, in general, non-steady-state conditions are not required to explain progressive  $^{34}\text{S}$  enrichment as long as the standing stock of secondarily precipitated sulfur is significantly  $^{34}\text{S}$ -depleted relative to in flowing sulfate (56), as would be expected with MSR (54, 55).

Interestingly, Marsiyandi River sulfate  $^{34}\text{S}$  and  $^{18}\text{O}$  values span nearly the entire range measured in rivers across the globe (Fig. 4). The majority of this isotope variability occurs within a single lithologic unit, the TSS, despite all evidence to suggest sulfate is quantitatively derived from pyrite oxidation. This observation implies that riverine sulfate  $^{34}\text{S}$  compositions are an insufficient conservative tracer to estimate pyrite vs. evaporite weathering contributions to global sulfate export (20, 56, 57). In the TSS alone, MSR appears to increase  $^{34}\text{S}$  by  $30\pm$  within consistently pyrite-dominated lithology; this would traditionally be interpreted as a shift from pyrite-dominated to evaporite-dominated weathering (57). Furthermore, downstream Marsiyandi River tributary isotope compositions approach median values for global data sets, suggesting that global  $^{34}\text{S}$  and  $^{18}\text{O}$  distributions may more strongly reflect MSR intensity and secondary sulfur storage in floodplains than weathering lithology.

Sulfate  $^{17}\text{O}$  trends corroborate the importance of MSR and secondary sulfur recycling in downstream catchments. Although the mass-dependent relationship describing MSR ( $\delta_{\text{MSR}}$ ) is poorly constrained, it likely lies between 0.5270 and 0.5305 (45). If we assume pyrite oxidation throughout the catchment generates primary sulfate with an isotope composition similar to that observed in high-elevation headwater

streams, then fractionation by MSR would lead to the observed increase in  $^{18}\text{O}$  as well as a slight decrease in  $^{17}\text{O}$  of residual sulfate (Fig. 3). Still, most downstream tributary data fall below the MSR fractionation line and imply secondary incorporation of  $^{17}\text{O}$ -depleted oxygen into sulfate, most likely from  $\text{O}_2$ .

Sulfate generated by MSR can be reoxidized either biotically or abiotically. Aerobic, chemolithoautotrophic sulfate oxidizing bacteria (SOB) are known to rapidly oxidize sulfide to sulfate in the presence of  $\text{O}_2$  (58). However, aerobic SOB likely utilize an electron transport chain rather than an oxygenase enzyme (59); resulting sulfate oxygen atoms are thus exclusively derived from  $\text{H}_2\text{O}$  and not from  $\text{O}_2$  directly (60). Alternatively, abiotic  $\text{H}_2\text{S}$  oxidation, while kinetically slower than oxidation by SOB (58), would directly incorporate  $\text{O}_2$  and could explain observed downstream trends. This mechanism MSR followed by secondary  $\text{H}_2\text{S}$  oxidation and abiotic  $\text{O}_2$  incorporation additionally reconciles our data with previous riverine sulfate  $^{17}\text{O}$  observations. Specifically, Mississippi River sulfate in Baton Rouge, Louisiana, USA displays a negative mean  $^{17}\text{O}$  of  $0.091 \pm 0.043\text{‰}$  VSMOW ( $n = 41$ ), which was previously interpreted to reflect tropospheric  $\text{O}_2$  contributions during pyrite oxidation (61). We instead interpret this result as reflecting continued secondary sulfur recycling, although the potential for alternative sulfate sources and anthropogenic inputs in the Mississippi River cannot be discounted (61).

If the mechanism proposed here is true more generally, then the locus of  $\text{O}_2$  incorporation into sulfate occurs not in erosive, pyrite-rich headwaters but rather during secondary sulfur recycling in lowland floodplains. This difference could carry implications for sulfate  $^{17}\text{O}$  compositions through geologic time.

**Conclusion and Implications for Earth History.** The utility of sulfate  $^{17}\text{O}$  as a paleo $\text{O}_2$  tracer is predicated on tropospheric  $\text{O}_2$  incorporation via oxidative pyrite weathering. In this study, we targeted highly erosive rivers draining pyrite-rich shale lithologies to isolate the  $^{17}\text{O}$  signature of pyrite oxidation-derived sulfate; results under modern conditions suggest a complex reaction network that does not directly incorporate  $\text{O}_2$ . However,  $\text{O}_2$  is the only major atmospheric species that carries a negative  $^{17}\text{O}$  anomaly; observed  $^{17}\text{O}$  values in Precambrian sulfate-bearing rocks therefore require atmospheric  $\text{O}_2$  incorporation into sulfate precursors (3, 8, 14, 15). Here we hypothesize that such incorporation may occur during secondary sulfur recycling in floodplains; this mechanism predicts that floodplain area could act as an additional, previously unrecognized control on sulfate  $^{17}\text{O}$  composition. Still, open questions remain regarding the interpretation of geologic sulfate  $^{17}\text{O}$  records, including the dependence of  $\text{ROS}^{17}\text{O}$  compositions on  $p\text{O}_2/p\text{CO}_2$  and the implications for paleo-atmospheric compositions. Answering these questions will require mechanistic studies in modern settings in addition to new, high-resolution  $^{17}\text{O}$  measurements of geologic sulfate throughout the Phanerozoic Eon.

## Materials and Methods

The materials and methods are summarized here; further details are provided in the Supporting Information.

**Isotope Measurements and Data Reporting.** Site location and sample collection details, as well as major ion,  $^{18}\text{O}/^{16}\text{O}$ , and  $^{34}\text{S}/^{32}\text{S}$  ana-

lytical procedures, have been described previously (20, 29, 33, 35). Sulfate  $^{17}\text{O}/^{16}\text{O}$  ratios were measured by laser fluorination by  $\text{F}_2$  coupled with isotope ratio mass spectrometry (IRMS) following Ref. (62). Uncertainty ( $\pm 1\text{‰}$ ) was taken as the long-term reproducibility of a suite of primary sulfate standards ( $\pm 0.016\text{‰}$ ). Isotope ratios are reported in conventional delta notation:

$$\delta^i\text{O} = \frac{i=16R_{\text{sample}}}{i=16R_{\text{standard}}} - 1 \quad 1000\text{‰}; \quad [3]$$

where  $i = 17, 18$  is the isotope of interest,  $i=16R$  is the  $^{i}\text{O}/^{16}\text{O}$  ratio, and Vienna Standard Mean Ocean Water (VSMOW) is the reference standard.  $^{34}\text{S}$  is similarly reported using Vienna Canyon Diablo Triolite (VCDT) as the reference standard. To quantify small deviations from the expected mass-dependent  $^{17}\text{O}-^{18}\text{O}$  relationship,  $^{17}\text{O}/^{16}\text{O}$  ratios are reported as

$$\delta^{17}\text{O} = \ln \frac{^{17}\text{O}}{^{16}\text{O}} + 1 \quad \text{RL} \quad \ln \frac{^{18}\text{O}}{^{16}\text{O}} + 1 \quad 1000\text{‰}; \quad [4]$$

where  $\text{RL} = 0.5305$  is the high-temperature equilibrium reference line mass law (63) and  $\ln$  indicates logarithmic notation (64). Isotope offsets between sulfate and concomitant water are reported as

$$\delta^{18}\text{O} = \delta^{18}\text{O}_{\text{SO}_4^{2-}} - \delta^{18}\text{O}_{\text{H}_2\text{O}}; \quad [5]$$

and

$$\delta^{17}\text{O} = \delta^{17}\text{O}_{\text{SO}_4^{2-}} - \delta^{17}\text{O}_{\text{H}_2\text{O}}; \quad [6]$$

All major ion concentrations and sulfate isotope compositions are reported in Table S1.

**Geospatial Analysis.** Geospatial data were analyzed using ArcGIS Desktop v10.6 (ESRI Corporation); results are reported in Table S2. Catchment areas and geomorphic parameters upstream of each sampling location were calculated using the NASA Shuttle Radar and Topography Mission global digital elevation model v3.0 (1 arc-second resolution). Glacier extent was calculated using the Randolph Glacier Inventory v6.0. Mean annual precipitation (MAP) and mean annual temperature (MAT) were calculated using the WorldClim v2 global climate database (30 second resolution) (65). Local elevation, slope, MAT, and MAP for each sample were taken as the value of the raster pixel underlying each sampling location. Catchment-averaged elevation, slope, MAP, and MAT were calculated as the mean value for all pixels within a given catchment area. Main-stem distance, elevation, and MAT profiles (Fig. 1B) were generated using the flow-accumulation river network and underlying raster pixels. Sample downstream distances were calculated as the main-stem path length from the headwater source to the main-stem point nearest to each sample location.

**Weathering Lithology Mixing Model.** For each sample, the relative proportions of solutes derived from weathering of different end-member lithologies were estimated using a conservative tracer mixing model. The end members considered in this model were: dolomite, evaporites, gneiss/granite, limestone, and shale. Although evaporite lithologies in general and gypsum in particular have not been reported in the Marsiyandi basin (26), we nonetheless included them in the model since their presence would add non-pyrite-derived  $\text{SO}_4^{2-}$ . Our calculated pyrite-derived  $\text{SO}_4^{2-}$  contributions are thus minimum estimates. The conservative tracers considered in this model were:  $\text{Ca}^{2+}$ ,  $\text{K}^+$ ,  $\text{Mg}^{2+}$ ,  $\text{Na}^+$ ,  $\text{Cl}^-$ ,  $\text{SO}_4^{2-}$ , and the constraint that all fractional contributions sum to unity. This model was solved using a Monte Carlo approach similar to that of Ref. (56). In addition to end-member contributions to each sample, this approach estimated a posteriori end-member conservative tracer ranges. Finally, the fraction of pyrite-derived  $\text{SO}_4^{2-}$  in each sample, termed  $f_{\text{py}}$ , was calculated as the relative proportion of shale weathering in that sample multiplied by the a posteriori  $\text{SO}_4^{2-}$  concentration for the shale end member. A priori and a posteriori end-member conservative tracer ranges are reported in Table S3.

## Major Isotope Compilation and Data Analysis

All published riverine sulfate  $^{34}\text{S}$  and  $^{18}\text{O}$  compositions, along with paired water  $^{18}\text{O}$  where available, were compiled from Refs.

537 (18–20, 57, 61, 66–70) (Table S4). Regression slopes were calculated  
538 using either weighted least squares regression if the ordinate is  
539 known perfectly (i.e., downstream distance; Fig. S1) or reduced  
540 major axis regression if the ordinate is known to contain uncertainty  
541 (i.e., isotope cross plots). Reported  $p$  values are the probability that  
542 regression slopes are statistically equal to zero and regressions with  
543  $p < 0.05$  are deemed significant. See Ref. (71) for regression details  
544 and equations.

545 **ACKNOWLEDGMENTS.** We thank Julien Föriél for laboratory  
546 assistance, Kevin Sutherland for helpful discussions on early versions  
547 of the manuscript, as well as the editor and two anonymous reviewers  
548 whose comments greatly improved the overall strength and clarity  
549 of this paper. This research was supported by NSF EAGER grant  
550 number EAR1839341, ACS PRF grant number 59455-ND2 (both  
551 to J.D.H. and D.T.J.) and NSF MGG grant number OCE-1821958  
552 (to D.T.J.).

553 1. Thiemens MH (2006) History and applications of mass-independent isotope effects. *Annu. Rev. Earth Planet. Sci.* 34:217–262.  
554 2. Lyons TW, Reinhard CT, Planavsky NJ (2014) The rise of oxygen in earth's early ocean and atmosphere. *Nature* 506:307–315.  
555 3. Bao H, et al. (2000) Anomalous  $^{17}\text{O}$  compositions in massive sulphate deposits on the earth. *Nature* 406:176–179.  
556 4. Bao H, Lyons J, Zhou C (2008) Triple oxygen isotope evidence for elevated  $\text{CO}_2$  levels after a neoproterozoic glaciation. *Nature* 453:504–506.  
557 5. Bao H, Fairchild IJ, Wynn PM, Spötl C (2009) Stretching the envelope of past surface environments: Neoproterozoic glacial lakes from svalbard. *Science* 323:119–122.  
558 6. Cao X, Bao H (2013) Dynamic model constraints on oxygen-17 depletion in atmospheric  $\text{O}_2$  after a snowball earth. *Proc. Nat. Acad. Sci.* 110:14546–14550.  
559 7. Crockford PW, et al. (2018) Triple oxygen isotope evidence for limited mid-proterozoic primary productivity. *Nature* 559:613–616.  
560 8. Crockford PW, et al. (2019) Claypool continued: Extending the isotopic record of sedimentary sulfate. *Chem. Geol.* 513:200–225.  
561 9. Yung LL, Lee AY, Irion FW, DeMore WB, Wen J (1997) Carbon dioxide in the atmosphere: Isotopic exchange with ozone and its use as a tracer in the middle atmosphere. *J. Geophys. Res. Atmos.* 102:10857–10866.  
562 10. Williamson MA, Rimstidt JD (1994) The kinetics and electrochemical rate-determining step of aqueous pyrite oxidation. *Geochim. Cosmochim. Ac.* 58:5443–5454.  
563 11. Rimstidt JD, Vaughan DJ (2003) Pyrite oxidation: A state-of-the-art assessment of the reaction mechanism. *Geochim. Cosmochim. Ac.* 67:873–880.  
564 12. Kohl I, Bao H (2011) Triple-oxygen-isotope determination of molecular oxygen incorporation in sulfate produced during abiotic pyrite oxidation (ph = 2–11). *Geochim. Cosmochim. Ac.* 75:1785–1798.  
565 13. Balci N, Shanks III WC, Mayer B, Mandernack KW (2007) Oxygen and sulfur isotope systematics of sulfate produced by bacterial and abiotic oxidation of pyrite. *Geochim. Cosmochim. Ac.* 71:3796–3811.  
566 14. Crockford PW, et al. (2016) Triple oxygen and multiple sulfur isotope constraints on the evolution of the post-marinoan sulfur cycle. *Earth Planet. Sci. Lett.* 435:74–83.  
567 15. Hodgkiss MS, Crockford PW, Peng Y, Wing BA, Horner TJ (2019) A productivity collapse to end earth's great oxidation. *Proceedings of the National Academy of Sciences* 116(35):17207–17212.  
568 16. Reedy BJ, Beattie JK, Lowson RT (1991) A vibrational spectroscopic  $^{18}\text{O}$  tracer study of pyrite oxidation. *Geochim. Cosmochim. Ac.* 55:1609–1614.  
569 17. Holmes PR, Crundwell FK (2000) The kinetics of the oxidation of pyrite by ferric ions and dissolved oxygen: An electrochemical study. *Geochim. Cosmochim. Ac.* 64:263–274.  
570 18. Calmels D, Gaillardet J, Brenot A, France-Lanord C (2007) Sustained sulfide oxidation by physical erosion processes in the mackenzie river basin: Climatic perspectives. *Geology* 35:1003–1006.  
571 19. Das A, Chung CH, You CF (2012) Disproportionately high rates of sulfide oxidation from mountainous river basins of taiwan orogeny: Sulfur isotope evidence. *Geophys. Res. Lett.* 39:L2404.  
572 20. Turchyn AV, Tipper ET, Galy A, Lo JK, Bickle MJ (2013) Isotope evidence for secondary sulfide precipitation along the marsyandi river, nepal, himalayas. *Earth Planet. Sci. Lett.* 374:36–46.  
573 21. Gu X, et al. (2020) Chemical reactions, porosity, and microfracturing in shale during weathering: The effect of erosion rate. *Geochimica et Cosmochimica Acta* 269:63–100.  
574 22. Leticariu L, Schimmelmann A, Pratt LM, Ripley EM (2007) Oxygen isotope partitioning during oxidation of pyrite by  $\text{H}_2\text{O}_2$  and its dependence on temperature. *Geochim. Cosmochim. Ac.* 71:5072–5088.  
575 23. Schoonen MA, Harrington AD, Laffers R, Strongin DR (2010) Role of hydrogen peroxide and hydroxyl radical in pyrite oxidation by molecular oxygen. *Geochimica et Cosmochimica Acta* 74(17):4971–4987.  
576 24. Savarino J, Thiemens MH (1999) Analytical procedure to determine both  $^{18}\text{O}$  and  $^{17}\text{O}$  of  $\text{H}_2\text{O}_2$  in natural water and first measurements. *Atmos. Environ.* 33:3683–3690.  
577 25. Savarino J, Thiemens MH (1999) Mass-independent oxygen isotope ( $^{16}\text{O}$ ,  $^{17}\text{O}$ ,  $^{18}\text{O}$ ) fractionation found in  $\text{H}_2\text{O}$ ,  $\text{O}_2$  reactions. *J. Phys. Chem. A* 103:9221–9229.  
578 26. Bordet P, et al. (1971) *Recherches Géologiques dans l'Himalaya du Népal, Région de la Thakkhola*. (Éd. du Centre Nat. de la Recherche Scientif.).  
579 27. Coleman M (1996) Orogen-parallel and orogen-perpendicular extension in the central nepalese himalayas. *Geol. Soc. Am. Bull.* 108:1594–1607.  
580 28. Searle MP, Godin L (2003) The south tibetan detachment and the manaslu leucogranite: A

structural reinterpretation and restoration of the annapurna-manaslu himalaya, nepal. *J. Geol.* 111:505–523. 616  
617  
29. Tipper ET, et al. (2006) The short term climatic sensitivity of carbonate and silicate weathering fluxes: Insight from seasonal variations in river chemistry. *Geochim. Cosmochim. Ac.* 70:2737–2754. 618  
619  
30. Bookhagen B, Burbank DW (2010) Toward a complete himalayan hydrological budget: Spatiotemporal distribution of snowmelt and rainfall and their impact on river discharge. *J. Geophys. Res. Earth Surf.* 115:F03019. 620  
621  
31. Le Fort P (1975) Himalayas: The collided range. present knowledge of the continental arc. *Am. J. Sci.* 275:1–44. 622  
623  
32. Sharp Z, Wostbrock J, Pack A (2018) Mass-dependent triple oxygen isotope variations in terrestrial materials. *Geochim. Perspect. Lett.* 7:27–31. 624  
625  
33. Becker JA, Bickle MJ, Galy A, Holland TJ (2008) Himalayan metamorphic  $\text{CO}_2$  fluxes: Quantitative constraints from hydrothermal springs. *Earth Planet. Sci. Lett.* 265:616–629. 626  
627  
34. Bickle MJ, et al. (2005) Relative contributions of silicate and carbonate rocks to riverine sr fluxes in the headwaters of the ganges. *Geochim. Cosmochim. Ac.* 69:2221–2240. 628  
629  
35. Tipper ET, Galy A, Bickle MJ (2008) Calcium and magnesium isotope systematics in rivers draining the himalaya-tibetan-plateau region: Lithological or fractionation control? *Geochim. Cosmochim. Ac.* 72:1057–1075. 630  
631  
36. Hemingway JD, et al. (2019) Glacier meltwater and monsoon precipitation drive upper ganges basin dissolved organic matter composition. *Geochim. Cosmochim. Ac.* 244:216–228. 632  
633  
37. Evans MJ, Derry LA, Anderson SP, France-Lanord C (2001) Hydrothermal source of radiogenic sr to himalayan rivers. *Geology* 29:803–806. 634  
635  
38. Galy A, France-Lanord C (1999) Weathering processes in the ganges–brahmaputra basin and the riverine alkalinity budget. *Chem. Geol.* 159:31–60. 636  
637  
39. Galy A, France-Lanord C, Derry LA (1999) The strontium isotopic budget of himalayan rivers in nepal and bangladesh. *Geochim. Cosmochim. Ac.* 63:1905–1925. 638  
639  
40. Fowler T, Holmes P, Crundwell F (1999) Mechanism of pyrite dissolution in the presence of *Thiobacillus ferrooxidans*. *Appl. Environ. Microbiol.* 65:2987–2993. 640  
641  
41. Lee CCW, Savarino J, Thiemens MH (2001) Mass independent oxygen isotopic composition of atmospheric sulfate: Origin and implications for the present and past atmosphere of earth and mars. *Geophys. Res. Lett.* 28:1783–1786. 642  
643  
42. Savarino J, Lee CC, Thiemens MH (2000) Laboratory oxygen isotopic study of sulfur (iv) oxidation: Origin of the mass-independent oxygen isotopic anomaly in atmospheric sulfates and sulfate mineral deposits on earth. *J. Geophys. Res. Atmos.* 105:29079–29088. 644  
645  
43. Johnson CA, Mast MA, Kester CL (2001) Use of  $^{17}\text{O}/^{16}\text{O}$  to trace atmospherically-deposited sulfate in surface waters: A case study in alpine watersheds in the rocky mountains. *Geophysical research letters* 28:4483–4486. 646  
647  
44. Duan K, Thompson L, Yao T, Davis M, Mosley-Thompson E (2007) A 1000 year history of atmospheric sulfate concentrations in southern asia as recorded by a himalayan ice core. *Geophysical Research Letters* 34:L01810. 648  
649  
45. Waldeck A, et al. (2019) Deciphering the atmospheric signal in marine sulfate oxygen isotope composition. *Earth Planet. Sci. Lett.* 522:12–19. 650  
651  
46. Wankel SD, Bradley AS, Eldridge DL, Johnston DT (2014) Determination and application of the equilibrium oxygen isotope effect between water and sulfite. *Geochim. Cosmochim. Ac.* 125:694–711. 652  
653  
47. Becker U, Rosso KM, Hochella Jr MF (2001) The proximity effect on semiconducting mineral surfaces: a new aspect of mineral surface reactivity and surface complexation theory? *Geochimica et Cosmochimica Acta* 65:2641–2649. 654  
655  
48. Helman Y, Barkan E, Eisenstadt D, Luz B, Kaplan A (2005) Fractionation of the three stable oxygen isotopes by oxygen-producing and oxygen-consuming reactions in photosynthetic organisms. *Plant Physiology* 138:2292–2298. 656  
657  
49. Cooper WJ, Lean D, Carey J (1989) Spatial and temporal patterns of hydrogen peroxide in lake waters. *Can. J. Fish. Aquat. Sci.* 46:1227–1231. 658  
659  
50. Mostafa KM, Sakugawa H (2009) Spatial and temporal variations and factors controlling the concentrations of hydrogen peroxide and organic peroxides in rivers. *Environ. Chem.* 6:524–534. 660  
661  
51. Michalski G, Scott Z, Kabling M, Thiemens MH (2003) First measurements and modeling of  $^{17}\text{O}$  in atmospheric nitrate. *Geophysical Research Letters* 30. 662  
663  
52. Kiel BA, Cardenas MB (2014) Lateral hyporheic exchange throughout the mississippi river network. *Nature Geoscience* 7:1–5. 664  
665  
53. Baier MA, Dahm CN, Valett HM (1999) Acetate retention and metabolism in the hyporheic zone of a mountain stream. *Limnology & Oceanography* 44:1530–1539. 666  
667  
54. Leavitt WD, Halevy I, Bradley AS, Johnston DT (2013) Influence of sulfate reduction rates on the phanerostrophic sulfur isotope record. *Proc. Nat. Acad. Sci.* 110:11244–11249. 668  
669  
55. Masterson A, Alperin MJ, Berelson WM, Johnston DT (2018) Interpreting multiple sulfur isotope signals in modern anoxic sediments using a full diagenetic model (california-mexico margin: Alfonso basin). *American Journal of Science* 318:459–490. 670  
671  
56. Torres MA, et al. (2016) The acid and alkalinity budgets of weathering in the andes–amazon system: Insights into the erosional control of global biogeochemical cycles. *Earth Planet. Sci. Lett.* 450:381–391. 672  
673  
57. Burke A, et al. (2018) Sulfur isotopes in rivers: Insights into global weathering budgets, pyrite oxidation, and the modern sulfur cycle. *Earth Planet. Sci. Lett.* 496:168–177. 674  
675  
58. Luther GW, et al. (2011) Thermodynamics and kinetics of sulfide oxidation by oxygen: a look at inorganically controlled reactions and biologically mediated processes in the environment. *Frontiers in microbiology* 2:62. 676  
677  
59. Van Stempvoort D, Krouse H (1994) Controls of  $^{18}\text{O}$  in sulfate: Review of experimental data and application to specific environments in *Environmental Geochemistry of Sulfide Oxidation*, eds. Alpers C, Blowes D. (ACS Publications, Washington, D.C.). 678  
679  
60. Suzuki I (1965) Incorporation of atmospheric oxygen-18 into thiosulfate by the sulfur-oxidizing enzyme of thiobacillus thiooxidans. *Biochimica et Biophysica Acta* 110:97–101. 680  
681  
61. Killingsworth BA, Bao H, Kohl IE (2018) Assessing pyrite-derived sulfate in the mississippi river with four years of sulfur and triple-oxygen isotope data. *Environ. sci. Technol.* 52:6126–6136. 682  
683  
684  
685  
686  
687  
688  
689  
690  
691  
692  
693  
694  
695  
696  
697  
698  
699

